



Enabling water-based processing of graphene/alumina composites using an infiltration approach with amphiphilic triblock copolymers

Guillermo Menendez^a, Thomas Kynaston^a, Ignacio J. Villar-Garcia^b, Min Gao^a, Sam L. Evans^a, Victoria G. Rocha^{a,c,*},¹

^a School of Engineering, Cardiff University, The Parade, 14 - 17, Cardiff CF24 3QE, UK

^b NAPP Endstation, CIRCE Beamline, ALBA Synchrotron, Carrer de la Llum, 2 - 26, Cerdanyola del Valles 08290, Spain

^c Instituto de Ciencia y Tecnología del Carbono (INCAR), Francisco Pintado Fe, 26, 33011, Spain

ARTICLE INFO

Keywords:

Graphene oxide
Ceramic-based composites
Freeze-casting
Spark plasma sintering
Materials processing

ABSTRACT

Enabling the direct infiltration of freeze-cast graphene structures with water-based ceramic suspensions, otherwise prevented by graphene's intrinsic hydrophobic behaviour, can lead to the production of hierarchical graphene/ceramic composites in a cost-effective and replicable manner. In this study, the addition of a triblock copolymer (PF127) in the formulation of water-based alumina slurries was used to allow the integration with reduced graphene oxide (rGO) scaffolds combining freeze-casting, wet chemistry processing and Spark Plasma Sintering. Wettability and infiltration tests were performed to optimise the composition of the ceramic suspension, leading to the preservation of alignment in embedded rGO scaffolds and maintaining channel widths of 5–15 μm upon sintering at 1500 °C.

1. Introduction

Ceramic-based composites have been widely explored to tackle the well-known weaknesses of pure ceramics (e.g. low fracture toughness and thermal fatigue) to enable their use in high-performing applications such as turbine blades, bearings, inert medical prostheses, and thermal or electrical insulators [1–3]. The outstanding combination of strength, lightweight and electrical/thermal properties characteristic of graphene (and graphene derivatives to a lesser extent) [4–6] has made it a promising reinforcement, with multiple studies demonstrating improvements in the properties of graphene/ceramic composites when compared to pure ceramics [7–10–13–16]. Most of these authors followed either traditional powder processing or colloidal and sol-gel solutions to integrate graphene in the ceramic material without carefully controlling the internal structure of the composite. Novel design concepts have alternatively taken inspiration from natural composites such as nacre, which tailor the internal hierarchy of the constituents at different length scales, applying it to processing of ceramic-based materials and maximising the combination of strength and toughness beyond the traditional rule of mixtures [1,17–20,21].

A promising technique aiming to support the creation of bioinspired

materials is freeze-casting, or ice-templating, a simple processing method for developing highly-porous materials obtained by controlled unidirectional solidification of an aqueous suspension of the target material. Its cost-effectiveness and versatility have made it an essential technique in the production of porous materials of different nature, from polymers, ceramics and metals to more complex macromolecules and biomaterials for the food industry [22–25,26] (More examples in the FreezeCasting.net database [27]). Graphene aerogels have also been obtained by freeze-casting using water/organic suspensions of graphene oxide (GO) as a precursor with tailored interlayer thickness and achieving high reproducibility [28–31,32].

One of freeze-casting's biggest prospects is its integration in ceramic-based composite manufacturing by combining different material pairs, namely ceramic/polymer [18,24,26], ceramic/ceramic [20,33] or ceramic/metal [21] hybrids. Graphene/ceramic composites following this approach have scarcely been presented, with two examples being the work from Wang et al. [34] and Picot et al. [31]. While in the former, the freeze-cast structure was made from combining GO and alumina in the precursor before hot-pressing, Picot et al. developed a separate rGO scaffold/infiltration approach in which the infiltrating ceramic phase consisted of polymer-derived ceramics (PDCs). Through this processing

* Corresponding author at: School of Engineering, Cardiff University, The Parade, 14 - 17, Cardiff CF24 3QE, UK.

E-mail address: vgarcia-rocha@incar.csic.es (V.G. Rocha).

¹ 0000-0001-6125-8556

<https://doi.org/10.1016/j.jeurceramsoc.2022.07.009>

Received 15 March 2022; Received in revised form 16 June 2022; Accepted 9 July 2022

Available online 15 July 2022

0955-2219/© 2022 The Authors. Published by Elsevier Ltd. This is an open access article under the CC BY-NC-ND license (<http://creativecommons.org/licenses/by-nc-nd/4.0/>).

route, a polymethyl siloxane polymer was used to infiltrate a freeze-cast graphene-like network, then converted to a glass ceramic (silicon oxy-carbide glass) via pyrolysis at 900°C and SPS at 1700°C. The substitution of the PDC matrix with advanced ceramics in the direct infiltration of graphene structures appears as a promising extension of this study, delivering a more cost-effective processing route without chemically converting the matrix material. However, this possibility cannot be achieved for water-based ceramic suspensions due to the hydrophobic nature of graphene, which repels the water solvent and prevents the integration of both materials.

One approach to overcoming this issue comes by adding a surfactant, such as an amphiphilic polymeric material. Pluronics are commercially labelled triblock copolymers containing polyoxyethylene (hydrophilic external chains) and polyoxypropylene (hydrophobic central chain) in the form of [PEO]*a*-[PPO]*b*-[PEO]*a*, known for their amphiphilic properties and thermoresponsive behaviour [35,36]. Pluronics have been conventionally used as surfactants [37] and drug-delivery carriers (0.5–2 wt% of solid material) in pharmaceuticals [38], recently explored in the robocasting field (15–25 wt% content) by exploiting their gelation capabilities in manufacturing 3D-printing inks [39–42]. Very recently, the amphiphilic capabilities of Pluronics have been approached in graphene/alumina systems to enhance the dispersion of the former and overcome the hydrophobicity barrier [43]. Pluronic F-127 (PF127) in particular has become a widespread selection because of its low toxicity and ability to reverse thermal gelation. Due to its combination of high molecular weight and large-sized hydrophobic PPO units, PF127 exhibits an adaptative rheological behaviour and tends to self-assemble into micelles upon reaching a critical concentration in suspension, leading to massive cross-linking at concentrations above 15 wt% at room temperature [36,44].

In this study, we explored the prospect of integrating PF127 in the formulation of water-based alumina slurries to modify the hydrophobic response of reduced GO aerogels and obtain graphene/ceramic composites through a scaffold-infiltration approach. We aim here to consolidate the roots of a promising, environmentally friendly processing route with growth potential in future works, paving the way towards manufacturing highly structured graphene/ceramic materials in a cost-effective and replicable manner.

2. Materials and methods

2.1. Materials

Water-based ceramic suspensions were prepared using commercial (Al₂O₃) alumina powder (Baikowski BA-15 W alpha alumina, specific surface area of 19.6 m² g⁻¹, particle size of 100 nm measured by SEM, density of 3.96 g cm⁻³ by helium pycnometry), grade-3 deionised (DI) H₂O and a triblock co-polymer based on polyoxyethylene (PEO) and polyoxypropylene (PPO) in the form of [PEO]*a*-[PPO]*b*-[PEO]*a* (*a* = 100, *b* = 65, Mw = 12600 g mol⁻¹, Sigma Aldrich) commercially labelled as Pluronic F-127 (PF127 in the text). Graphene oxide (GO) suspension (1 wt% GO, from GOGraphene, William Blythe Ltd.) was selected as the graphene precursor. 10 wt% solution of polyvinyl alcohol (PVA) in DI H₂O and pure sucrose powder (Sigma Aldrich) were used as a binder and enhancer of surface properties respectively [28,29,45].

2.2. Production of hierarchical reduced graphene oxide scaffolds

Commercial 1 wt% GO suspension was further diluted to 0.25 and 0.5 wt% GO concentration by adding DI H₂O. Sucrose and 10 wt% solution of PVA additives (50 wt% of GO content in the mixture) were included in the suspension and homogenised via speed-mixing using a DAC 800.1 FVZ Mixer at 1950 rpm for 8 min. GO suspensions were cast in Teflon/PLA moulds of various geometries using a custom-built freeze-casting setup [Supplementary Figure 1] similar to previous

works in the field [29–31], leading to cylindrical lab-sized (13 mm diameter, 18 mm height) and scaled-up aerogels (30 mm diameter and 33 mm height). After freezing the GO suspensions at 5°C min⁻¹ rate, ice sublimation was carried out by freeze-drying (Lablyo –85 Frozen in Time Ltd) below –60°C under 12 Pa vacuum for a minimum of 48 h depending on specimen size. A preliminary drying stage was applied overnight under 80°C inside a fan-circulated oven (LTE Scientific Raven Oven 2). Thermal reduction of GO aerogels (rGO) was performed in a Carbolite MTF 12/38/400 tubular furnace at three 1 h intermediate stages (100, 150 and 200°C) and a final isothermal stage at 900°C. The samples were placed in an alumina crucible (99% purity) and under a 2 lpm argon flow (Pureshield 11-W, 11.01 m³) to ensure a non-oxidising atmosphere.

2.3. Wettability study of alumina slurries on reduced graphene oxide films

A preliminary evaluation of wettability between GO and/or rGO (400°C) films and Al₂O₃/PF127 slurries was performed by contact angle (CA) measurements via sessile drop on an Attension Theta Lite optical tensiometer. GO films were spin-coated onto 10 x 10 mm silicon substrates (Graphenea, SiO₂/Si 300 nm) with a Laurell Spin coater WS-650–23 unit from a 0.37 wt% GO suspension. The spin-coated GO films were thermally annealed in a tubular furnace at three 30 min isothermal stages of 100, 250 and 400°C, reached at 2.5°C min⁻¹ heating rates to preserve the integrity of the films.

Al₂O₃/PF127 slurries were produced by first preparing 5 and 15 wt% PF127 stock solutions in DI H₂O. The alumina powder was then added up to the selected solid loading (0.1–1–5–12.5–25 wt% in H₂O) and PF127/Al₂O₃ wt./wt. ratio, speed-mixed for 10 min to maximise homogenisation. Gelation of these slurries was not expected as the PF127 content in H₂O did not exceed 5 wt%. Slurry droplets were deposited on GO and rGO films, evaluating the CA by averaging left and right angles throughout the first 10 s of deposition with the change of alumina solid content in suspension. Dynamic evaluation of the droplet spreading confirmed the CA did not change substantially during this period.

2.4. Graphene/alumina composites green bodies

The PF127/Al₂O₃ ratio in alumina slurries was adjusted through custom infiltration tests. 5.2 ± 0.2 mg cm⁻³ GO aerogels (freeze-cast from 0.25 wt% GO suspension) were annealed at 900°C, carefully deposited on top of the alumina slurries and monitored using a Nikon D5100 camera. The infiltration of 2/3 of the aerogel volume was selected as the endpoint to compare different tests and compensate for uncontrolled factors such as tilting, surface flatness and inaccuracies from the camera positioning. The graphene/alumina green bodies were produced by infiltrating rGO scaffolds originally cast from 0.5 wt% GO suspensions (28 mm diameter, 32 mm height and 3.7 ± 0.1 mg cm⁻³ in apparent density) with 25 wt% PF127/Al₂O₃ slurries and freeze-drying for further 72 h.

2.5. Consolidation of graphene/alumina composite

Spark Plasma Sintering (SPS) of graphene/alumina green bodies was performed in a Type HP D 10-SD unit from FCT Systeme GmbH. Freeze-dried infiltrated rGO scaffolds were placed in a 20 mm graphite die perpendicular to the pressure direction in the chamber and protected using graphite foil (0.3 mm thickness). The SPS cycles were performed under vacuum at 1500°C for 3 minutes, reached at a 100°C min⁻¹ heating rate based on previous works on the field [9]. Heating was controlled by a 10–5–12–2 current pulse sequence (ON time - OFF time - number of pulses - extra pause, respectively). Uniaxial pressure was linearly increased up to 50 MPa, maintained during the isothermal stage and quickly released down to contact force during cooling. The cooling rate was also limited to 50°C min⁻¹ to reduce the thermal stress induced in the ceramic material in the process and prevent cracking of

the discs.

2.6. Characterisation techniques

GO lateral size was averaged by elliptical fitting of 100 single flakes after dilution of the GO suspension to 500 ppm in isopropanol and drop-cast on silicon substrates. Examination of the flakes was performed via optical microscopy (OM) under polarised light. The apparent density of cylindrical freeze-cast scaffolds was evaluated by dividing their weight and volume (3-point averages of height and diameter measured with a digital calliper). A Micromeritics AccuPyc 1330 pycnometer was used to obtain the density of the BA-15 W raw alumina powder.

Freeze-dried GO suspensions were characterised through Thermogravimetric Analysis (TGA), X-ray Photoelectron Spectroscopy (XPS), Raman spectroscopy and X-ray Diffraction (XRD) before and after thermal reduction. TGA was performed in a Mettler Toledo TGA/DSC 3 + up to 1000°C on a 5°C min⁻¹ heating rate under nitrogen atmosphere. XPS was performed in a Thermo Fisher Scientific K-alpha+ spectrometer using a micro-focused monochromatic Al X-ray source (72 W) providing an analysis defining elliptical X-ray spot of approximately 400 x 600 μm. Data was recorded at pass energies of 150 eV for survey scans (1 eV step size) and 40 eV for high resolution scan (0.1 eV step size), interpreted using CasaXPS software. Shirley or two-point linear background subtractions were employed depending on background shape. All peaks were fitted using GL(30) lineshapes, a combination of a Gaussian (70%) and Lorentzian (30%) apart from the carbon sp² component fitted with an asymmetric function (LF (0.75,1.15,100,150)) to account for the natural shape of this spectral line. The C1s sp² component was fitted with an FWHM of 0.9 ± 0.05 eV at 284.1 eV binding energy. The rest of the sp³ and carbonyl groups were set with FWHM of 2 ± 0.5 eV to account for the different types of substitutions within the GO and additives in some samples, giving rise to a mixture of chemical environments.

The Raman spectra of GO before and after annealing was obtained with a Renishaw inVia Raman microscope using a 514 nm laser (5% power) with standard grating, an exposure time of 10 s and three accumulations per sample. X-ray Diffraction (XRD) was performed with a Siemens Diffraktometer D5000 and processed with HighScore Xpert Plus software. The viscosity (cP) of the Al₂O₃/PF127 suspensions was measured using a Fungilab rotational viscometer under a rotation speed range of 5–250 rpm and an average spindle torque of 50–80% at 20°C. Two low-viscosity spindles (TL5 and TL6) from a small-sample spindle set were used in the measurements. Both the alignment of reduced GO aerogels and the fracture surface from sintered graphene/ceramic composites was verified by Field-emission Scanning Electron Microscopy (FESEM) on a ZEISS 1540 XB unit, under an EHT of 5 kV, 5 mm working distance and an in-lens detector. ImageJ software was used to process the graphs and figures presented in this study, using the FigureJ extension for the arrangement of microscopy images [46].

3. Results and discussion

3.1. Partially reduced graphene scaffolds

GO colloidal suspensions can deliver hierarchical graphene networks based on their extremely high dispersibility and affinity with a water solvent. Increasing the GO concentration and flake size of the suspension can trigger its self-ordering behaviour, leading to the formation of liquid crystal phases [47]. The mean lateral size of GO flakes in the suspension used was 8 ± 2 μm (Fig. 1). These dimensions, along with the selected GO concentration of 0.25–0.5 wt%, sit in the range in which a nematic LC phase can be formed [48] and preserved by the controlled directional freezing performed via freeze-casting.

The effect of thermal annealing in the GO precursor was first evaluated. Elemental analysis confirmed a shift of the C/O atomic ratio from 0.9 to 48.8 after reduction at 900°C, indicating the removal of most

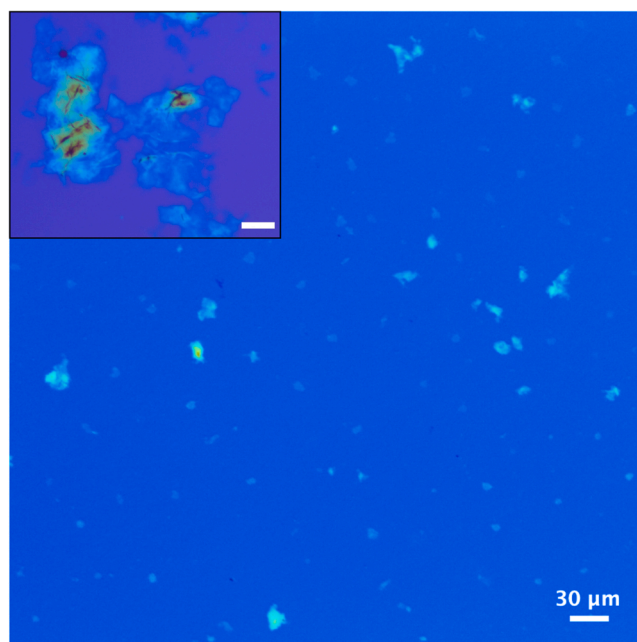


Fig. 1. Optical microscopy of GO flakes distributed on a silicon substrate. Inset: Close-up of GO flakes exhibiting the change in colouring with flake agglomeration (Scale bar: 5 μm).

oxidised groups attached to the former GO sheets. Nitrogen and sulphur impurities (1.60 and 1.78 at%, respectively) were also found in the analysis, expected from the heavy oxidation process during the GO synthesis. The XPS spectra of the freeze-dried GO:PVA:sucrose formulation (labelled as freeze dried GO suspension in Fig. 2) before and after annealing was studied. This formulation required for the freeze casting processing includes PVA:sucrose:GO with a 0.5:0.5:1 mass ratio. The presence of PVA:sucrose increases the content of C-O groups, not as present in GO films [Supplementary Figure 2] in favour of carbonyl C = O [31,49].

After the thermal treatment, the general survey provided a C/O change from 2.34 to 49.26 supporting the elimination of oxidised groups. Analysis of the C1s spectra also confirmed the sp²:sp³ hybridisation ratio increased from 0.24 to 7.36 after reduction at 900°C, with a significant depletion of epoxide (C-O), carbonyl (C = O) and carboxyl (O-C = O) groups present in the graphene sheets. The increase in sp² carbon concentration after reduction resulted in satellite features at higher energies, as represented by the plasmon features at 291 and 293 eV in the rGO graph.

TGA measurements also reflected the effect of thermal treatment in the precursor [Supplementary Figure 3], showing a weight reduction of almost 60% for GO at 900°C, with rGO only losing 10% of the original weight at this temperature. D and G Raman peaks were found at 1354 and 1588 cm⁻¹ in GO, with a slight shift to 1358 and 1597 cm⁻¹ upon annealing [Supplementary Figure 4]. A D/G intensity ratio of 0.88 and 0.99 was obtained before and after the annealing, respectively. The Raman spectra did not reflect a significant change in the intensity ratio displayed as expected for the low temperature of annealing selected [50]. The evolution of D/G ratio upon thermal treatment is more complex in oxidised graphene than in pure graphene or other graphitic sp² systems. In the latter, a reduction of D band intensity (lowering the D/G ratio) would be associated with a decrease in the number of defects in the structure [51][52]. However, as the carbon from GO is mostly in sp³ hybridisation within a highly disordered structure, thermal annealing is also expected to restore the sp² graphitic domains, hence increasing the D/G ratio [53][54]. XRD analysis confirmed a shift from a sharper 2θ peak around 10° into a broader peak at 20–25° after thermal annealing of the GO [Supplementary Figure 5], which verifies the partial

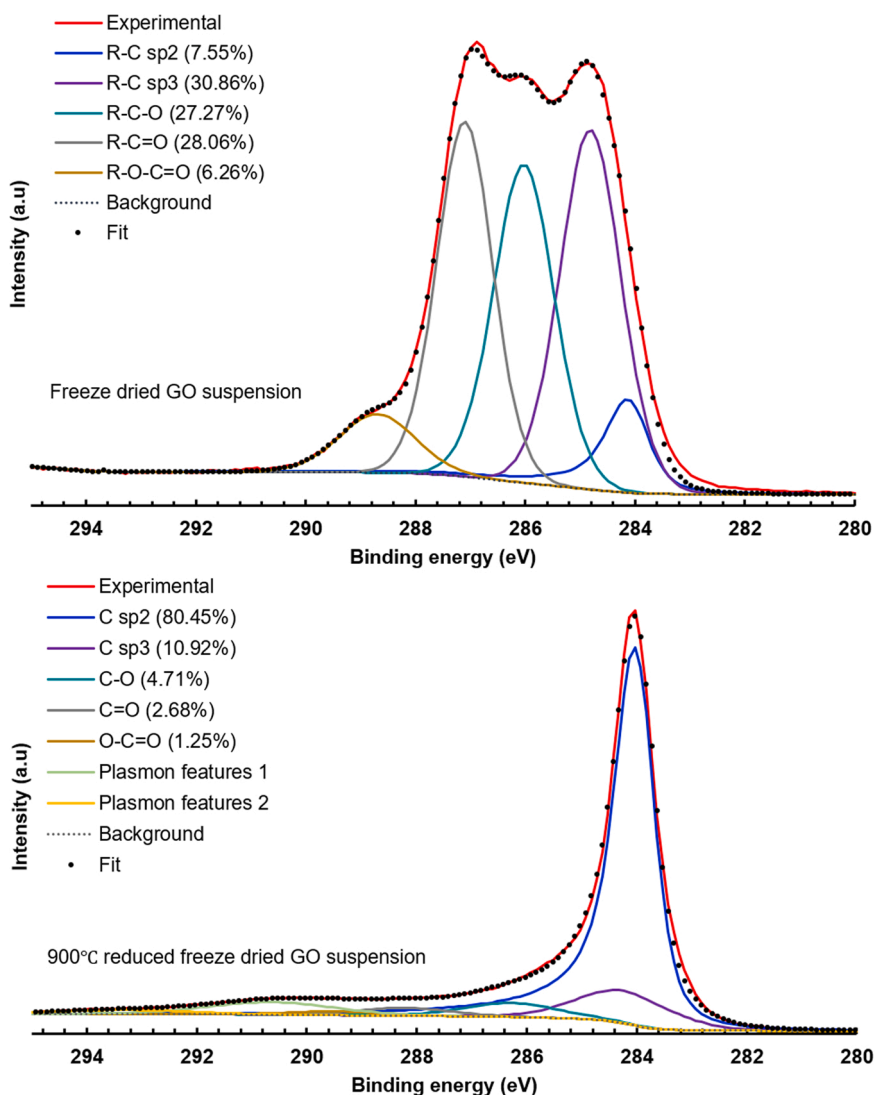


Fig. 2. XPS analysis showing the C1s spectra of freeze-dried GO suspensions before partial reduction (Top graph) and after partial reduction at 900°C (Bottom graph). The suspensions also contained PVA:sucrose additions included for freeze-casting.

graphitisation of the material in agreement with the literature [50].

GO aerogels in various sizes and shapes were produced by exploiting the flexibility of the freeze-casting technique. The aerogels were reduced by thermal annealing in a non-oxidising atmosphere to restore the sp^2 domains and avoid combustion at high temperature. Slow heating rates and intermediate stages below 200°C were applied to prevent structural disruption caused by the removal of water-labile molecules. The cross-section of the aerogels exhibited a typical honeycomb-like pattern, maintaining a unidirectionally aligned structure with 15–30 μm channel widths (Fig. 3a,b,c). FESEM characterisation also confirmed a significant loss of alignment in aerogels produced from 0.25 wt% GO suspensions [Supplementary Figure 6] compared to 0.5 wt% GO, which was attributed to the reduced lateral size of the GO precursor employed. While cylindrical upscaled rGO aerogels of 28 mm diameter and 32 mm height (Fig. 3e) could be produced maintaining the 0.5 wt% GO concentration in suspension and freezing rates, lab-sized specimens (13 mm diameter, 18 mm height of $2.8 \pm 0.2 \text{ mg cm}^{-3}$ in apparent density) were first made for infiltration testing to accelerate the soaking process and permit batch freeze-drying and annealing (Fig. 3d).

3.2. Wettability study

Static contact angle (CA) tests were designed to evaluate the effect of adding PF127 to the alumina slurries of low-medium solid loading (0.1–1–5–12.5–25 wt% Al_2O_3) in the wettability. To provide more consistent CA values, flat GO spin-coated films were selected as the graphene phase instead of the freeze-cast scaffolds, comparing with and without partial annealing up to 400°C under vacuum. Due to the delicate nature of the spin-coated films, lower temperatures were selected to achieve a compromise between an effective removal of functional groups present in the GO sheets [55] and damaging the continuity of the film, exposing the silicon substrate underneath as a result of excessive temperature. The consistency of the annealed GO film was verified by FESEM, confirming the GO coating exhibited sufficient thickness to prevent the underlying silicon substrate from affecting the obtained CA. At the substrate edges, the advancing front of the film was still visible (Fig. 4a), which was avoided during deposition of the alumina slurries.

XPS analysis of the GO films also confirmed the low annealing temperature of 400°C was sufficient to reduce the film partially [Supplementary Figure 2]. The oxygen contribution in the general XPS survey was lowered from 30.6 to 15.9 at% upon annealing of the films, supporting the partial elimination of functional groups decorating the graphene flakes. The atomic $sp^2:sp^3$ hybridisation ratio in the C1s

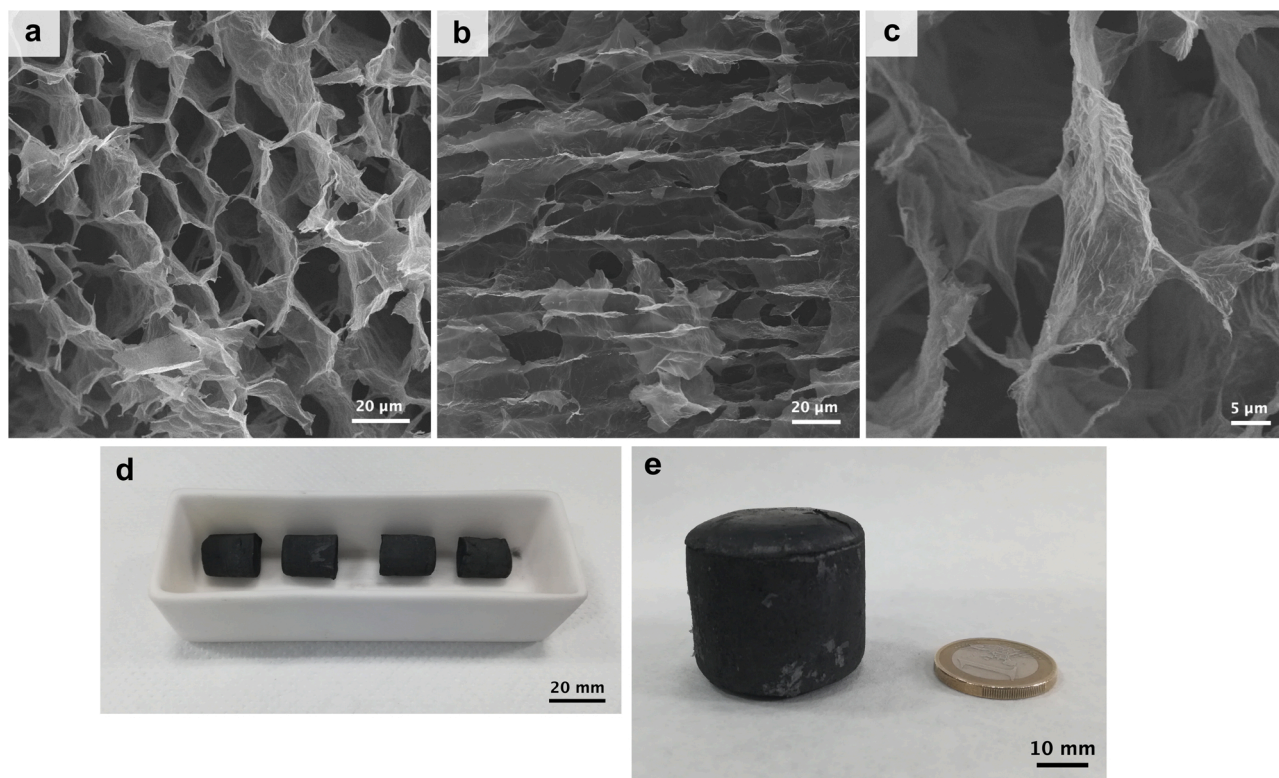


Fig. 3. FESEM images of (a) perpendicular and (b) parallel cross-section of freeze-cast $3.7 \pm 0.1 \text{ mg cm}^{-3}$ rGO aerogels along the freezing direction, taken after thermal annealing at 900°C exhibiting $15\text{--}30 \mu\text{m}$ channel widths in a honeycomb-like structure. (c) Closer picture of rGO flakes suspended in the freeze-cast structure. (d) Array of rGO aerogels (13 mm diameter, 18 mm height) after batch annealing prepared for infiltration tests. (e) Scaled-up rGO aerogel (30 mm diameter, 25 mm height).

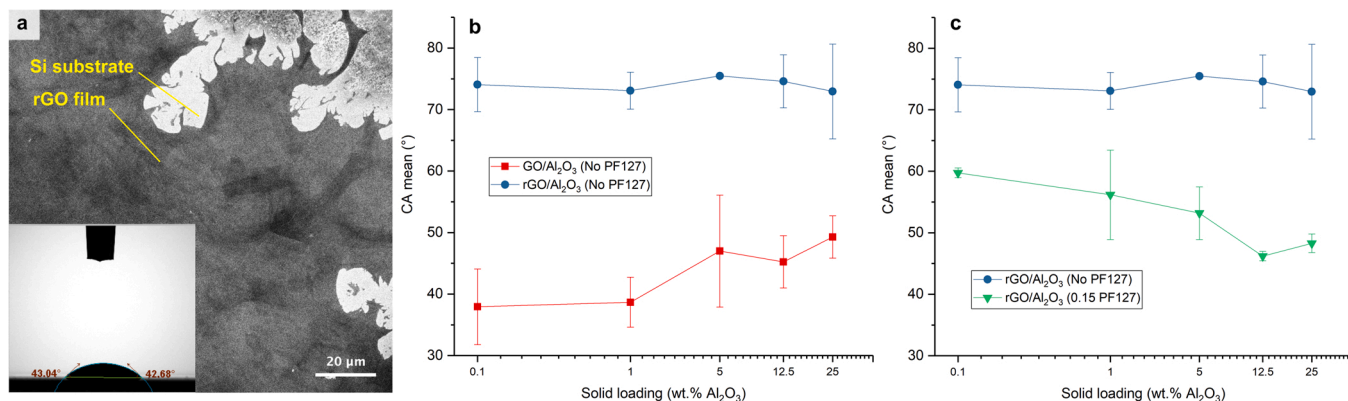


Fig. 4. (a) FESEM image of spin-coated GO films on a silicon substrate showing the advancing front of the film. Inset: Cross-section of 1 wt% Al₂O₃ droplet deposited on a GO film during tensiometer measurements. (b) Average contact angle (CA) of Al₂O₃ droplets with increasing solid loading (0.1–25 wt%) on GO and rGO (400°C) films in the absence of PF127 additions. (c) Average contact angle (CA) of Al₂O₃/PF127 droplets with increasing Al₂O₃ solid loading (0.1–25 wt%) under a fixed 0.15 PF127/Al₂O₃ ratio on GO and rGO (400°C) films.

spectra also increased from 0.12 to 2.63 after the carbonisation step, highlighting the partial restoration of the sp^2 graphitic domains although lower than in rGO annealed at 900°C . The plasmon features of the spectrum at higher energies were also less prominent, given the lower concentration of sp^2 carbon. A significant reduction of carbonyl (from 50.3 to 8.0 at%) and carboxyl content (from 7.9 to 2.3 at%) was found in the GO films compared to the XPS survey previously performed for freeze-dried GO (from Fig. 2), with slight deviations in the binding energy positions associated with these groups. These were attributed to the high variability of functional groups provided from PVA:sucrose additions in the previous GO suspensions envisioned for freeze-casting.

Without any PF127 addition, wettability of the alumina slurries

shifted from a $35\text{--}50^\circ$ range to a $70\text{--}75^\circ$ range against the GO films before and after partial annealing (Fig. 4b). This increase in film hydrophobicity was expected from the depletion of sp^3 carbon and carbon-oxygen links in GO films along with a higher presence of sp^2 carbon after annealing. Although far from the super-hydrophobic behaviour reported for graphene nanoplatelets and fully-reduced GO sheets around $120\text{--}150^\circ$ [56], partial reduction at 400°C proved sufficient to modify the droplet response, with a sharper change expected for rGO aerogels annealed at 900°C . As the Al₂O₃ loading increased to 12.5 and 25 wt%, the obtained CAs were progressively higher, reflecting the influence of solid loading in the slurries.

A significant change in wettability was obtained after adding PF127

in the alumina slurries, drawing the behaviour of rGO films closer to that of GO films before reduction (Fig. 4c). Measured CA averages of rGO/Al₂O₃ droplets with PF127 decreased when increasing the alumina solid content of the suspension. The amphiphilic effect of the copolymer addition was intensified in the 12.5–25 wt% Al₂O₃ solid content range. In this loading range, the effect of annealing on the GO film was negligible, with barely any difference in the reported CAs for GO before and after annealing (Fig. 4b,c). This similar behaviour could be explained by the larger quantity of PF127 in the alumina droplet, interacting equally with both the hydrophilic oxidised groups of GO and the hydrophobic regions of sp² carbon. It should be recognised that this drop in hydrophobicity would not only be derived from the increase of alumina content but also from the increase of PF127 content in the slurry, which arises from maintaining an equal PF127/Al₂O₃ ratio in these measurements.

At higher solid loadings, the ceramic droplet could also be pinned due to increased viscosity, limiting its spread on the film. The viscosity of 12.5 and 25 wt% alumina loading suspensions was evaluated for increasing PF127/Al₂O₃ wt./wt. ratios of 0, 0.07 and 0.15 (Fig. 5), with

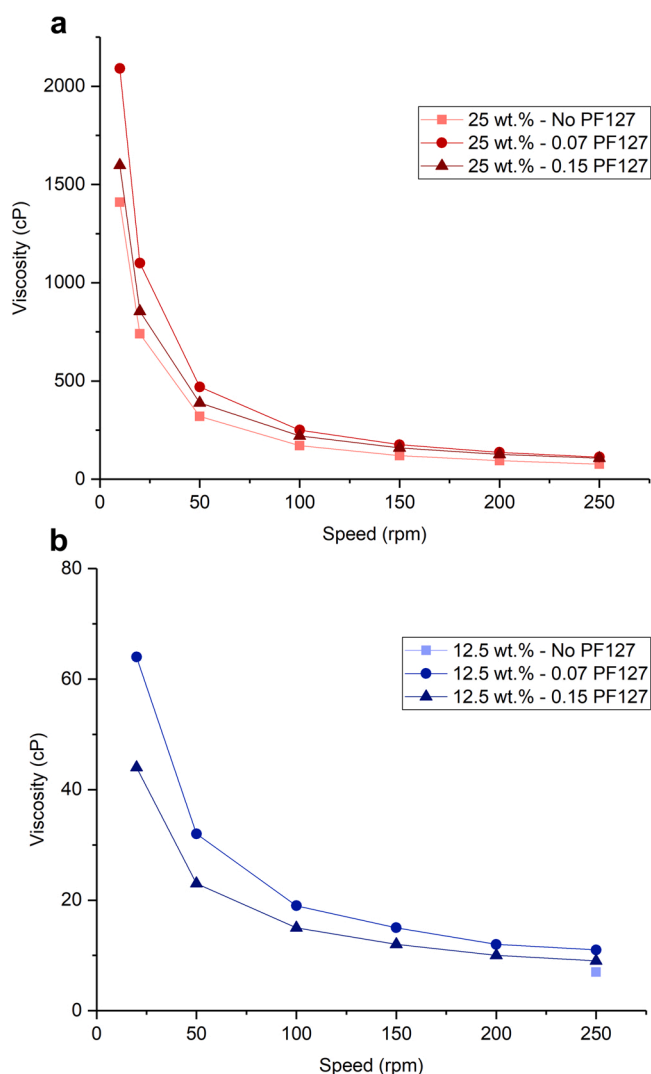


Fig. 5. Rotational viscosity measurements of alumina slurries at increasing PF127/Al₂O₃ ratios (0, 0.07 and 0.15) for (a) 25 wt% and (b) 12.5 wt% solid loadings. Two different spindles were used for each graph due to the difference in viscosity range (TL6 in top vs. TL5 in bottom). The viscosity of 12.5 wt% slurries without PF127 was found at the lower torque limit of the TL5 spindle at highest speeds, for which only one point could be included in the graph.

a 0.15 ratio representing 0.15 mg of PF127 for every 1 mg of Al₂O₃. Although all suspensions exhibited similar shear-thinning behaviour, the increase in alumina solid loading accompanied a remarkable increase in viscosity. This effect was most noticeable at lower speeds, which resulted in a sharper change in viscosity up to the 1000–2000 cP range (Fig. 5a). The additions of PF127 in suspension appeared to have a mixed effect on the viscosity. While smaller additions (0.07 ratio) seemed to increase the overall viscosity of the suspension slightly, bigger additions (0.15 ratio) resulted in a reduction of viscosity to an in-between point, which could denote a better integration of the additive in suspension. The overall viscosity of alumina slurries appeared not to have been as significantly affected by changes in PF127 content as by changes in the alumina solid loading, which was considered for the infiltration tests in the next section.

3.3. rGO scaffold infiltration

The formulation of PF127/alumina mixtures was further optimised by testing the infiltration capabilities of thermally reduced freeze-cast GO aerogels instead of flat GO or rGO films. Temperature, volume of ceramic suspension and size/density of the rGO aerogel were kept constant in the study of infiltration by different PF127/Al₂O₃ wt./wt. ratio.

The parameters selected for the infiltration test are displayed in Fig. 6a, highlighting the PF127/Al₂O₃ wt./wt. ratios tested from 0 to 0.15 and the increase of total PF127 content in the suspension. Each set of conditions was tested three times on similar cylindrical rGO aerogels (13 mm diameter, 18 mm height, 2.8 ± 0.2 mg cm⁻³). In these tests, the alumina solid loading was maintained at 12.5 wt%, as higher viscosity in the suspension (from Fig. 5) hindered the infiltration of smaller aerogels when deposited on top of the ceramic slurry directly.

In water-based alumina slurries without any PF127 additions, infiltration was never achieved because of the hydrophobic behaviour of reduced GO aerogels. At 0.01 PF127/Al₂O₃ ratio in suspension the infiltration was moderately improved, reaching the infiltration endpoint of 2/3 of the aerogel volume after 3–4 minutes (Fig. 6b). However, infiltration was never complete under these conditions, with suspensions also appearing unstable after freezing due to alumina sedimentation. Starting from a PF127/Al₂O₃ ratio of 0.03, the soaking of the rGO aerogel was greatly enhanced, achieving the infiltration endpoint in less than 40 seconds. From this point onward the trend changed completely, obtaining progressively reduced times of infiltration up to 0.15 PF127/Al₂O₃ ratios (Fig. 6c). The amount of PF127 material in the composite should be reduced to the minimum necessary without eliminating its positive effect, as the copolymer will be released during the sintering stage, potentially damaging the envisioned structure of the graphene/ceramic composite. Through these infiltration tests, the effect of PF127 in solution was verified, hinting towards 0.03 as the minimum PF127/Al₂O₃ ratio for the main processing route (Fig. 6b). However, 0.07–0.15 ratios were selected for allowing the infiltration of suspensions of higher loading (above 12.5 wt%) and larger rGO aerogels to deliver a homogeneous green body composite.

SPS discs with a minimum of 3 mm in height were required to produce specimens with sufficient thickness for future mechanical testing. From the volume limitation of using cylindrical 30 mm graphitic dies during SPS, a minimum loading of 25 wt% in the infiltrating alumina slurry was required to provide sufficient solid material (calculated as roughly 8 g of alumina). Even though 0.07 PF127/Al₂O₃ ratios appeared sufficient to permit infiltration based on previous tests on lab-scale aerogels, the infiltration of larger scaffolds was expected to be negatively affected by the viscosity shift presented in Fig. 5 after increasing the alumina loading to 25 wt% in the slurry. Above 12.5 wt% loading, infiltration was achieved through preliminary wetting of the rGO scaffolds with ceramic slurry drops until complete soaking, instead of depositing the aerogel on top of the slurry as in Fig. 6c. After these adjustments, scaled-up rGO aerogels (28 mm

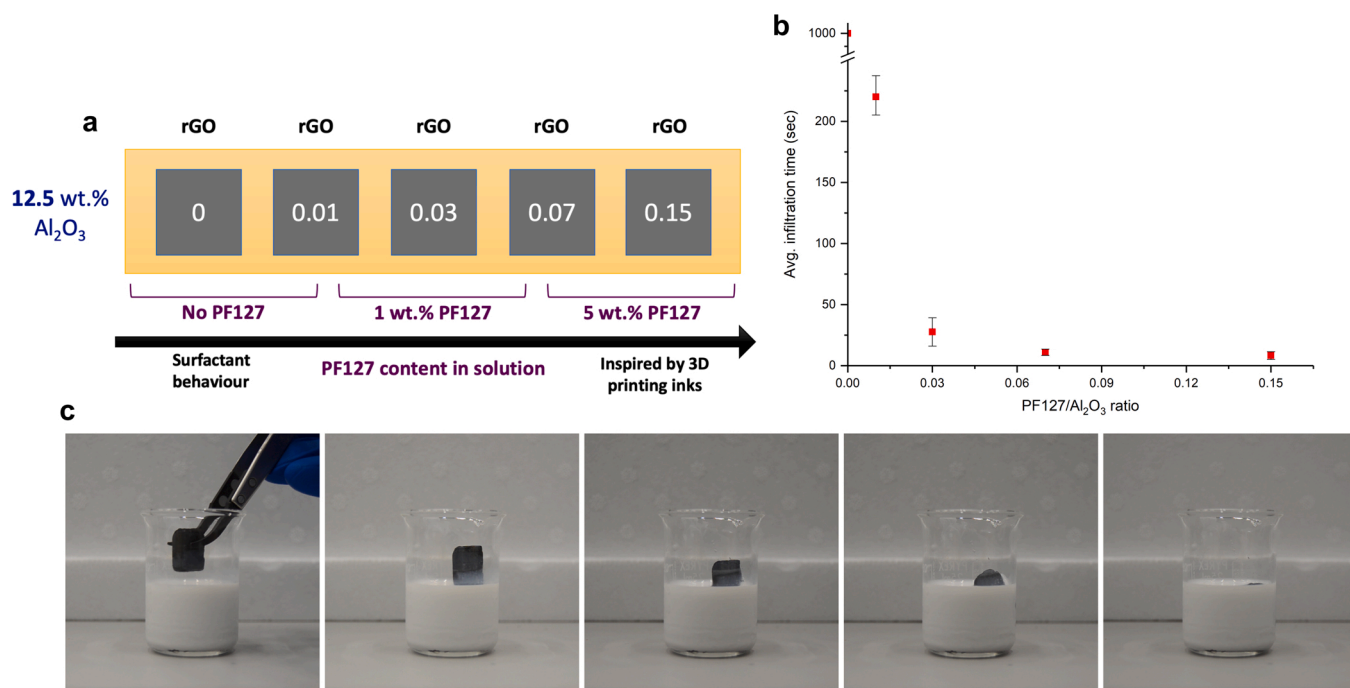


Fig. 6. (a) Schematic of infiltration test conditions, highlighting the increase in PF127 content in solution and the PF127/Al₂O₃ wt./wt. ratio for each case (0–0.15). (b) Infiltration time versus PF127/Al₂O₃ ratio in suspension (0–0.15), each case averaged for 3 analogous rGO aerogels. (c) Display of stages from aerogel deposition in suspension to complete infiltration (In the example, rGO aerogel on a 0.15 PF127/Al₂O₃ suspension).

diameter, 32 mm height and $3.7 \pm 0.1 \text{ mg cm}^{-3}$ in apparent density) were successfully infiltrated in 25 wt% Al₂O₃ suspensions containing 0.15 PF127/Al₂O₃ ratio and later freeze-dried prior to consolidation via SPS.

3.4. Graphene/alumina composite consolidation by SPS

SPS parameters (Methods section 2.5) were selected based on previous works on ceramic discs, especially on graphene/alumina composites [8,9,14,57]. Even though 1300–1350°C sintering temperatures could be sufficient to produce densified alumina discs, the effect of both a second graphitic phase embedded in the sample and the release of the remaining PF127 additive should be considered in the heat and pressure distributions during consolidation. Higher temperatures also account for better restoration of the electrical properties in the graphitic network, for which a temperature of 1500°C was eventually selected, with further optimisation required in future works.

The fracture surface of sintered rGO/alumina discs was examined by FESEM (Fig. 7). The freeze-cast structure of reduced GO scaffolds

embedded in the alumina matrix verified the preservation of the alignment after consolidation and validated the effectiveness of infiltration. The alumina matrix was found fully sintered at 1500°C with a mean grain size of $0.97 \pm 0.2 \mu\text{m}$ (measured by averaging 30 grains) compared to the 100 nm particle size of the original alumina powder. These values appeared slightly lower than $1.2 \pm 0.3 \mu\text{m}$ obtained for bulk alumina powder sintered at 1500°C without embedded graphene, which could be related to a grain boundary pinning effect of the rGO sheets limiting the alumina grain growth during sintering [Supplementary Figure 7]. Graphene additions have been reported to help with grain refinement of ceramic matrices sintered through SPS, preventing excessive growth that would otherwise be detrimental for the properties of the composite [43,58]. After exploring several fracture sections in the composite, the scaffold channel spacing ranged from 5 to 15 μm depending on the examination area. The cylindrical shape of the rGO aerogel could lead to stress concentrations under SPS pressing, with localised areas of the composite subjected to bigger compression selectively reducing the channel width. Another explanation could lie in a non-homogeneous infiltration of alumina material during previous

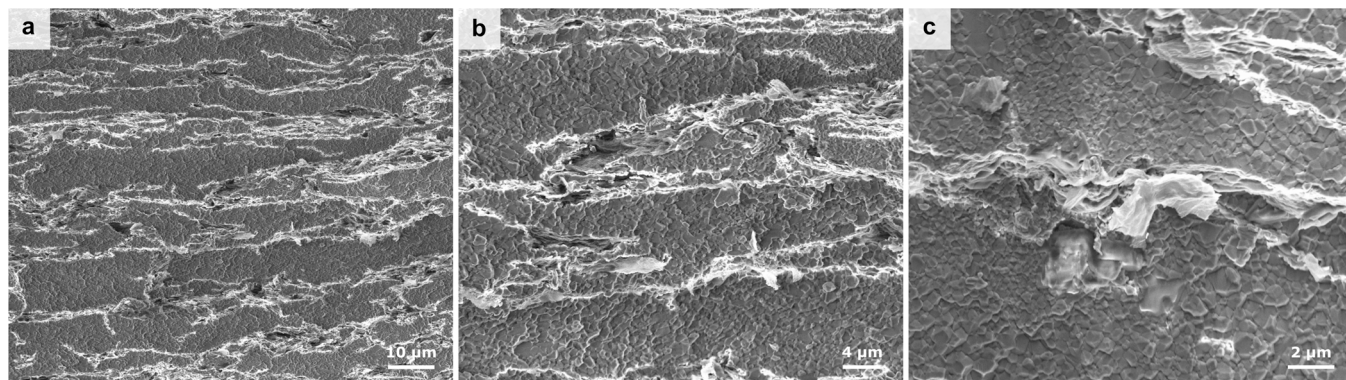


Fig. 7. FESEM images showing the fracture surface of rGO/alumina composites, sintered by SPS at 1500°C. (a) and (b) Preservation of alignment of the rGO scaffolds (5–15 μm channel width) embedded in the alumina matrix. (c) Focused image on pull-out of graphene flakes at the fracture surface.

steps, which would explain the gaps in the ceramic matrix found upon sintering as shown in Fig. 7b.

Pull-out of rGO flakes along the fracture surface was also confirmed in the microscope (Fig. 7c), which could contribute as extrinsic mechanisms in deflecting crack propagation and increase the fracture toughness of the composite material. Despite scaffolds constituting 1 wt % of the total weight, graphene agglomerates were found after examining the fracture surface of the composite. Limiting the GO content and producing scaffolds of lower density is essential to reduce agglomeration while maintaining the unidirectional alignment provided by freeze-casting [29]. The relatively low GO lateral flake size of $8 \pm 2 \mu\text{m}$ (previously shown in Fig. 1a) prevented from lowering the GO concentration in suspension below 0.5 wt% without a significant loss of alignment in the scaffolds during the freeze-casting stage. As discussed, an adequate GO precursor plays an essential role in the rheological properties of the suspension and the formation of liquid crystal phases [48]. The selection of custom-made GO suspensions with $20 + \mu\text{m}$ lateral size would directly improve the proposed processing route, reducing the presence of agglomerates while limiting the graphene content in the final composite.

Future steps also include targeting the scalability of the process by producing larger samples. Scaling-up is still needed to enable the production of specimens for mechanical testing, increasing the SPS graphite die size and evaluating the mechanical properties via strength and R-curve measurements.

4. Conclusions

The addition of a triblock copolymer (PF127) in the formulation of water-based alumina slurries provides a remarkable improvement in the wettability with ultra-light hydrophobic rGO aerogels. PF127/ Al_2O_3 content in suspension below 0.15 wt./wt. can enable the infiltration with freeze-cast rGO scaffolds that is otherwise unachievable, leading to highly structured graphene/ceramic composites obtained through the combination of wet-chemistry processing and sintering. The freeze-cast scaffold's alignment was preserved after composite consolidation, maintaining a graphene interconnected network with channel widths below $15 \mu\text{m}$. This study presents the basis of a promising water-based processing route to produce ceramic-based composites with limited graphene inclusions (1 wt%), with high prospects for obtaining superior mechanical capabilities and added functionalities.

Declaration of Competing Interest

The authors declare that they have no known competing financial interests or personal relationships that could have appeared to influence the work reported in this paper.

Acknowledgements

The authors would like to thank the financial support provided by the Engineering and Physical Sciences Research Council (EPSRC: EP/N509449/1) and Cardiff University. We extend the gratitude to the JECS Trust for the award given to attend the 43rd International Conference and Exposition on Advanced Ceramics and Composites (ICACC19) and the Winter Workshop at Daytona Beach, Florida organised by the American Ceramic Society (ACerS). V.G. Rocha would like to thank the Spanish Government (Ramón y Cajal fellowship, RYC2018–024404-I) and the support from the Spanish Research Agency AEI/PID2019–104028RB-I00.

Appendix A. Supporting information

Supplementary data associated with this article can be found in the online version at doi:10.1016/j.jeurceramsoc.2022.07.009.

References

- [1] R.O. Ritchie, The conflicts between strength and toughness, *Nat. Mater.* 10 (2011) 817, <https://doi.org/10.1038/nmat3115>.
- [2] K.T. Faber, T. Asefa, M. Backhaus-Ricoult, R. Brow, J.Y. Chan, S. Dillon, W. G. Fahrenholtz, M.W. Finnis, J.E. Garay, R.E. García, Y. Gogotsi, S.M. Haile, J. Halloran, J. Hu, L. Huang, S.D. Jacobsen, E. Lara-Curzio, J. LeBeau, W.E. Lee, C. G. Levi, I. Levin, J.A. Lewis, D.M. Lipkin, K. Lu, J. Luo, J.P. Maria, L.W. Martin, S. Martin, G. Messing, A. Navrotsky, N.P. Padture, C. Randall, G.S. Rohrer, A. Rosenflanz, T.A. Schaedler, D.G. Schlom, A. Schirring, A.J. Stevenson, T. Tani, V. Tikare, S. Trolrier-McKinstry, H. Wang, B. Yildiz, The role of ceramic and glass science research in meeting societal challenges: report from an NSF-sponsored workshop, *J. Am. Ceram. Soc.* 100 (2017) 1777–1803, <https://doi.org/10.1111/jace.14881>.
- [3] V.T. Rathod, J.S. Kumar, A. Jain, Polymer and ceramic nanocomposites for aerospace applications, *Appl. Nanosci.* 7 (2017) 519–548, <https://doi.org/10.1007/s13204-017-0592-9>.
- [4] V. Singh, D. Joung, L. Zhai, S. Das, S.I. Khondaker, S. Seal, Graphene based materials: past, present and future, *Prog. Mater. Sci.* 56 (2011) 1178–1271, <https://doi.org/10.1016/j.pmatsci.2011.03.003>.
- [5] A. Geim, K. Novoselov, The rise of graphene, *Nat. Mater.* 6 (2007) 183–191, <https://doi.org/10.1038/nmat1849>.
- [6] C. Gómez-Navarro, M. Burghard, K. Kern, Elastic properties of chemically derived single graphene sheets, *Nano Lett.* 8 (2008) 2045–2049, <https://doi.org/10.1021/nl801384y>.
- [7] K. Wang, Y. Wang, Z. Fan, J. Yan, T. Wei, Preparation of graphene nanosheet/alumina composites by spark plasma sintering, *Mater. Res. Bull.* 46 (2011) 315–318, <https://doi.org/10.1016/j.materresbull.2010.11.005>.
- [8] J. Liu, H. Yan, M.J. Reece, K. Jiang, Toughening of zirconia/alumina composites by the addition of graphene platelets, *J. Eur. Ceram. Soc.* 32 (2012) 4185–4193, <https://doi.org/10.1016/j.jeurceramsoc.2012.07.007>.
- [9] A. Centeno, V.G. Rocha, B. Alonso, A. Fernández, C.F. Gutierrez-Gonzalez, R. Torrecillas, A. Zurutuza, Graphene for tough and electroconductive alumina ceramics, *J. Eur. Ceram. Soc.* 33 (2013) 3201–3210, <https://doi.org/10.1016/j.jeurceramsoc.2013.07.007>.
- [10] M. Belmonte, A. Nistal, P. Boutbien, B. Román-Manso, M.I. Osendi, P. Miranzo, Toughened and strengthened silicon carbide ceramics by adding graphene-based fillers, *Scr. Mater.* 113 (2016) 127–130, <https://doi.org/10.1016/j.scriptamat.2015.10.023>.
- [11] L. Liu, Y. Wang, X. Li, L. Xu, X. Cao, Y. Wang, Z. Wang, C. Meng, W. Zhu, X. Ouyang, Enhancing toughness in boron carbide with reduced graphene oxide, *J. Am. Ceram. Soc.* 99 (2016) 257–264, <https://doi.org/10.1111/jace.13943>.
- [12] C. Zhang, A. Nieto, A. Agarwal, Ultrathin graphene tribofilm formation during wear of Al_2O_3 -graphene composites, *Nanomater. Energy* 5 (2016) 1–9, <https://doi.org/10.1016/j.nma.2015.02.007>.
- [13] C.F. Gutierrez-Gonzalez, A. Smirnov, A. Centeno, A. Fernández, B. Alonso, V. G. Rocha, R. Torrecillas, A. Zurutuza, J.F. Bartolome, Wear behavior of graphene/alumina composite, *Ceram. Int.* 41 (2015) 7434–7438, <https://doi.org/10.1016/j.ceramint.2015.02.061>.
- [14] L.S. Walker, V.R. Marotto, M.A. Rafiee, N. Koratkar, E.L. Corral, Toughening in graphene ceramic composites, *ACS Nano* 5 (2011) 3182–3190, <https://doi.org/10.1021/nn200319d>.
- [15] C. Ramirez, M.I. Osendi, Toughening in ceramics containing graphene fillers, *Ceram. Int.* 40 (2014) 11187–11192, <https://doi.org/10.1016/j.ceramint.2014.03.150>.
- [16] B. Lee, M.Y. Koo, S.H. Jin, K.T. Kim, S.H. Hong, Simultaneous strengthening and toughening of reduced graphene oxide/alumina composites fabricated by molecular-level mixing process, *Carbon* 78 (2014) 212–219, <https://doi.org/10.1016/j.carbon.2014.06.074>.
- [17] F. Barthelat, R. Rabiei, Toughness amplification in natural composites, *J. Mech. Phys. Solids* 59 (2011) 829–840, <https://doi.org/10.1016/j.jmps.2011.01.001>.
- [18] E. Munch, M.E. Launey, D.H. Alsem, E. Saiz, A.P. Tomsia, R.O. Ritchie, R.O. Alsem, Tough, bio-inspired hybrid materials, *Science* 322 (2008) 1516–1520, <https://doi.org/10.1126/science.1164865>.
- [19] M.E. Launey, E. Munch, D.H. Alsem, H.B. Barth, E. Saiz, A.P. Tomsia, R.O. Ritchie, Designing highly toughened hybrid composites through nature-inspired hierarchical complexity, *Acta Mater.* 57 (2009) 2919–2932, <https://doi.org/10.1016/j.actamat.2009.03.003>.
- [20] F. Bouville, E. Maire, S. Meille, B. Van De Moortèle, A.J. Stevenson, S. Deville, Strong, tough and stiff bioinspired ceramics from brittle constituents, *Nat. Mater.* 13 (2014) 508–514, <https://doi.org/10.1038/nmat3915>.
- [21] A. Wat, J. Lee, C.W. Ryu, B. Gludovatz, J. Kim, A. Tomsia, T. Ishikawa, J. Schmitz, A. Meyer, M. Alfreider, D. Kiener, E. Park, R. Ritchie, Bioinspired nacre-like alumina with a bulk metallic glass-forming alloy as a compliant phase, *Nat. Commun.* 10 (2019) 961, <https://doi.org/10.1038/s41467-019-08753-6>.
- [22] S. Deville, Ice-templating, freeze casting: Beyond materials processing, *J. Mater. Res.* 28 (2013) 2202–2219, <https://doi.org/10.1557/jmr.2013.105>.
- [23] Q. Cheng, C. Huang, A.P. Tomsia, Freeze casting for assembling bioinspired structural materials, *Adv. Mater.* (2017) 29, <https://doi.org/10.1002/adma.201703155>.
- [24] S. Deville, E. Saiz, R.K. Nalla, A.P. Tomsia, Freezing as a path to build complex composites, *Science* 311 (2006) 515–518, <https://doi.org/10.1126/science.1120937>.
- [25] H. Zhang, A.I. Cooper, Aligned porous structures by directional freezing, *Adv. Mater.* 19 (2007) 1529–1533, <https://doi.org/10.1002/adma.200700154>.

- [26] H. Zhang, I. Hussain, M. Brust, M. Butler, S. Rannard, A. Cooper, Aligned two- and three-dimensional freezing of polymers and nanoparticles, *Nat. Mater.* 4 (2005) 787–793, <https://doi.org/10.1038/nmat1487>.
- [27] K. Scotti, D. Dunand, Freeze casting - a review of processing, microstructure and properties via the open data repository, *freezecasting.net*, *Prog. Mater. Sci.* 94 (2018) 243–305, <https://doi.org/10.1016/j.pmatsci.2018.01.001>.
- [28] S. Barg, F.M. Perez, N. Ni, P. DoValePereira, R.C. Maher, E. Garcia-Tuñon, S. Eslava, S. Agnoli, C. Mattevi, E. Saiz, Mesoscale assembly of chemically modified graphene into complex cellular networks, *Nat. Commun.* (2014) 5, <https://doi.org/10.1038/ncomms5328>.
- [29] N. Ni, S. Barg, E. Garcia-Tunon, F. MacUlperez, M. Miranda, C. Lu, C. Mattevi, E. Saiz, Understanding mechanical response of elastomeric graphene networks, *Sci. Rep.* (2015) 5, <https://doi.org/10.1038/srep13712>.
- [30] E. D'Elia, S. Barg, N. Ni, V.G. Rocha, E. Saiz, Self-healing graphene-based composites with sensing capabilities, *Adv. Mater.* 27 (2015) 4788–4794, <https://doi.org/10.1002/adma.201501653>.
- [31] O.T. Picot, V.G. Rocha, C. Ferraro, N. Ni, E. D'Elia, S. Meille, J. Chevalier, T. Saunders, T. Peijs, M.J. Reece, E. Saiz, Using graphene networks to build bioinspired self-monitoring ceramics, *Nat. Commun.* (2017) 8, <https://doi.org/10.1038/ncomms14425>.
- [32] L. Qiu, J.Z. Liu, S.L. Chang, Y. Wu, D. Li, Biomimetic superelastic graphene-based zirconia composite, *Nat. Commun.* 3 (2012) 1241, <https://doi.org/10.1038/ncomms2251>.
- [33] G. Liu, T.W. Button, The effect of particle size in freeze casting of porous alumina-zirconia composite, *Ceram. Int.* 39 (2013) 8507–8512, <https://doi.org/10.1016/j.ceramint.2013.02.101>.
- [34] L. Wang, J. Bi, W. Wang, Y. Chen, R. Liu, X. Sun, Microstructure and mechanical properties of nacre-like alumina toughened by graphene oxide, *Ceram. Int.* 45 (2019) 8081–8086, <https://doi.org/10.1016/j.ceramint.2019.01.013>.
- [35] A. turcov, P. Schmidt, J. Dybal, Role of hydration and water coordination in micellization of pluronic block copolymers, *J. Colloid Interface Sci.* 352 (2010) 415–423, <https://doi.org/10.1016/j.jcis.2010.07.077>.
- [36] V. Lenaerts, C. Triqueneaux, M. Quartern, F. Rieg-Falson, P. Couvreur, Temperature-dependent rheological behavior of pluronic f-127 aqueous solutions, *Int. J. Pharm.* 39 (1987) 121–127, [https://doi.org/10.1016/0378-5173\(87\)90206-7](https://doi.org/10.1016/0378-5173(87)90206-7).
- [37] J. Orth, W.H. Meyer, C. Bellmann, G. Wegner, Stabilization of aqueous -al2o3 suspensions with block copolymers, *Acta Polym.* 48 (1997) 490–501, <https://doi.org/10.1002/actp.1997.010481105>.
- [38] J.J. Escobar-Chávez, M. López-Cervantes, A. Naik, Y. Kalia, D. Quintanar-Guerrero, A. Ganem-Quintanar, Applications of thermo-reversible pluronic f-127 gels in pharmaceutical formulations, *J. Pharm. Pharm. Sci.* (2006).
- [39] J. Franco, P. Hunger, M. Launey, A. Tomsia, E. Saiz, Direct write assembly of calcium phosphate scaffolds using a water-based hydrogel, *Acta Biomater.* 6 (2010) 218–228, <https://doi.org/10.1016/j.actbio.2009.06.031>.
- [40] M. Müller, J. Becher, M. Schnabelrauch, M. Zenobi-Wong, Nanostructured pluronic hydrogels as bioinks for 3d bioprinting, *Biofabrication* 7 (2015), 035006, <https://doi.org/10.1088/1758-5090/7/3/035006>.
- [41] E. Feilden, E.G.T. Blanca, F. Giuliani, E. Saiz, L. Vandeperre, Robocasting of structural ceramic parts with hydrogel inks, *J. Eur. Ceram. Soc.* 36 (2016) 2525–2533, <https://doi.org/10.1016/j.jeurceramsoc.2016.03.001>.
- [42] V.G. Rocha, E. García-Tuñón, C. Botas, F. Markoulidis, E. Feilden, E. D'Elia, N. Ni, M. Shaffer, E. Saiz, Multimaterial 3d printing of graphene-based electrodes for electrochemical energy storage using thermoresponsive inks, *ACS Appl. Mater. Interfaces* 9 (2017) 37136–37145, <https://doi.org/10.1021/acsami.7b10285>.
- [43] X. Fan, N. Ni, X. Wang, W. Hao, F. Guo, X. Zhao, Mechanically isotropic alumina prepared by spark plasma sintering: the role of pyrolytic carbon and multilayer graphene, *J. Eur. Ceram. Soc.* 41 (2021) 4242–4251, <https://doi.org/10.1016/j.jeurceramsoc.2021.01.056>.
- [44] M. Jalaal, G. Cottrell, N. Balmforth, B. Stoerber, On the rheology of pluronic f127 aqueous solutions, *J. Rheol.* 61 (2017) 139–146, <https://doi.org/10.1122/1.4971992>.
- [45] E. Munch, E. Saiz, A.P. Tomsia, S. Deville, Architectural control of freeze-cast ceramics through additives and templating, *J. Am. Ceram. Soc.* 92 (2009) 1534–1539, <https://doi.org/10.1111/j.1551-2916.2009.03087.x>.
- [46] J. Mutterer, E. Zinck, Quick-and-clean article figures with figurej, *J. Microsc.* 252 (2013) 89–91, <https://doi.org/10.1111/jmi.12069>.
- [47] B. Dan, N. Behabtu, A. Martinez, J.S. Evans, D.V. Kosynkin, J.M. Tour, M. Pasquali, I.I. Smalyukh, Liquid crystals of aqueous, giant graphene oxide flakes, *Soft Matter* 7 (2011) 11154–11159, <https://doi.org/10.1039/C1SM06418E>.
- [48] Al-Zangana, S., Iliut, M., Turner, M., Vijayaraghavan, A., Dierking, L., 2017. Confinement effects on lyotropic nematic liquid crystal phases of graphene oxide dispersions 4, 041004.10.1088/2053-1583/aa843a.
- [49] S. Stankovich, D.A. Dikin, R.D. Piner, K.A. Kohlhaas, A. Kleinhammes, Y. Jia, Y. Wu, S.T. Nguyen, R.S. Ruoff, Synthesis of graphene-based nanosheets via chemical reduction of exfoliated graphite oxide, *Carbon* 45 (2007) 1558–1565, <https://doi.org/10.1016/j.carbon.2007.02.034>.
- [50] S.H. Huh, Thermal reduction of graphene oxide, *InTech*, 2011, <https://doi.org/10.5772/14156>.
- [51] A.C. Ferrari, J.C. Scardaci, V. Casiraghi, C. Piscanec, M. Meyer, F. Roth, S. Lazzeri, D. Mauri, K.S. Jiang, S. Novoselov, A.K. Geim, Raman spectrum of graphene and graphene layers, *Phys. Rev. Lett.* (2006) 97, <https://doi.org/10.1103/PhysRevLett.97.187401>.
- [52] Y. Zhang, X. Li, Bioinspired, graphene/al2o3 doubly reinforced aluminum composites with high strength and toughness, *Nano Lett.* 17 (2017) 6907–6915, <https://doi.org/10.1021/acs.nanolett.7b03308>.
- [53] S. Eigler, C. Dotzer, A. Hirsch, Visualization of defect densities in reduced graphene oxide, *Carbon* 50 (2012) 3666–3673, <https://doi.org/10.1016/j.carbon.2012.03.039>.
- [54] S. Pei, H.M. Cheng, The reduction of graphene oxide, *Carbon* 50 (2012) 3210–3228, <https://doi.org/10.1016/j.carbon.2011.11.010>.
- [55] F. Kim, L.J. Cote, J. Huang, Graphene oxide: surface activity and two-dimensional assembly, *Adv. Mater.* 22 (2010) 1954–1958, <https://doi.org/10.1002/adma.200903932>.
- [56] X. Zhang, S. Wan, J. Pu, L. Wang, X. Liu, Highly hydrophobic and adhesive performance of graphene films, *J. Mater. Chem.* 21 (2011) 12251, <https://doi.org/10.1039/c1jm12087e>.
- [57] T. He, J. Li, L. Wang, J. Zhu, W. Jiang, Preparation and consolidation of alumina/graphene composite powders, *Mater. Trans.* 50 (2009) 749–751, <https://doi.org/10.2320/matertrans.MRA2008458>.
- [58] A. Nieto, A. Bisht, D. Lahiri, C. Zhang, A. Agarwal, Graphene reinforced metal and ceramic matrix composites: a review, *Int. Mater. Rev.* 62 (2017) 241–302, <https://doi.org/10.1080/09506608.2016.1219481>.